Effect of Inclusions and Microstructural Characteristics on the Mechanical Properties and Fracture Behavior of a High-Strength Low-Alloy Steel

A. Ray, S.K. Paul, and S. Jha

The strength and toughness properties of hot-rolled plates from three commercial heats of a high-strength low-alloy steel were investigated with respect to their intrinsic microstructural and inclusion characteristics. One heat was argon purged and contained relatively higher carbon and sulfur, whereas the other two heats, with lower carbon and sulfur levels, were sulfide shape controlled. The study revealed that although yield and tensile strengths specific to a heat were unaffected by testing direction, the anisotropy in tensile ductility was greater in steels with stringered sulfides. Despite similar grain sizes in all the steels, Charpy shelf energy and impact transition temperature were significantly affected by pearlite content and sulfide morphology and to a lesser extent by pearlite banding. The modification of stringer sulfides to tiny lenticular/globular oxysulfides resulted in considerably higher shelf energies, lowering of impact transition temperatures, and minimal anisotropy of impact properties. The macroscopic appearance of splitting on the fracture surfaces of transverse Charpy specimens associated with low impact energies confirmed failure by a low-energy mode. The presence of pancake-shaped ferrite grains and fractographic evidence of inclusion stringers inside furrows identified their role in accentuating the splitting phenomenon.

Keywords
impact energy, inclusions, pearlite banding, splitting phenomenon

1. Introduction

ALTHOUGH THE influence of nonmetallic inclusions on the ductility and toughness of steel is recognized (Ref 1-4), it nevertheless remains a subject of continuous exploration. Although the yield and ultimate tensile strengths of steels remain largely unaffected, the ductility, particularly in the transverse and short-transverse directions, is intimately related to both the volume fraction as well as the morphology of inclusions (Ref 1). Inclusions, such as sulfides and silicates, which tend to be elongated during hot rolling, are usually responsible for drastic reductions in ductility (Ref 5). In microscopic levels, nonmetallic inclusions are responsible for the creation of microvoids, leading to microcracking by their coalescence (Ref 6).

Nonmetallic inclusions in commercial steels can be classified into three different groups:

1. Macroscopic inclusions of exogenous origin and larger than several hundred microns in size
2. Microscopically small inclusions, visually assessed for cleanliness rating, in the size range from a few microns to 100 μm
3. Inclusions of submicroscopic size, such as spherical oxides

Inclusions belonging to classes 2 and 3 are by far the most predominant in steel. The ductility of steel is mainly influenced by inclusions of optical microscopic size (class 2), especially by stringers of MnS and silicates. The existence of elongated inclusions, such as MnS, results in the formation of inclusion-size cracks that consequently act as strain concentrators, bringing about final separation by localized shearing. A change in inclusion morphology from elongated to globular shape and a decrease in the volume fraction of inclusions greatly improve ductility.

The toughness of steel as measured by Charpy V-notch (CVN) impact energy has an exponential relation with the inclusion volume percent (Ref 4). The effects of inclusions are exercised through their size, shape, volume fraction, and distribution. Nonmetallic inclusions that are elongated during hot rolling, such as MnS in aluminum-killed steels, markedly reduce the impact energy in the transverse direction, giving rise to anisotropy (Ref 7, 8). The effect of nonmetallic inclusions on the impact transition temperature (ITT), however, has not been clearly established. According to some investigators (Ref 9), there is no significant effect of inclusions on ITT, while others (Ref 10) have observed a noticeable effect.

The present study was undertaken to examine the effect of inclusion and microstructural characteristics on the tensile and impact properties and the fracture behavior of high-strength low-alloy (HSLA) steel plates used for forming chassis members of heavy-duty vehicles. The plates investigated were hot rolled and had a minimum yield strength of 38 kg/mm^2.

2. Experimental Method

Full-width plate samples (7 mm thick and 1010 mm wide) from three different commercial heats of an HSLA steel were selected for complete characterization. The chemical analyses of these plates are given in Table 1. All three heats were made

A. Ray, S.K. Paul, and **S. Jha,** Physical Metallurgy Group, Research and Development Centre for Iron and Steel, Steel Authority of India Limited, Ranchi-834002, India.

Table 1 Composition of hot-rolled steel plates

Heat No.	Element, wt%							
	C	Mn	P	S	Si	Al	Nb	Ti
1	0.12	0.96	0.029	0.034	0.05	0.056	0.07	...
2	0.08	0.51	0.009	0.006	0.14	0.045	0.022	...
3	0.09	1.25	0.011	0.005	0.05	0.037	0.026	0.018

Table 2(a) Tensile properties of hot-rolled steel plates of different heats (half-width position)

Heat No.	Orientation	Yield strength, kg/mm^2	Tensile strength, kg/mm^2	Uniform elongation, %	Total elongation on 50 mm GL, %	YS/UTS
1	L	41.14	50.85	18.0	31.6	0.81
	T	43.52	51.46	16.0	26.4	0.84
	X	42.84	52.55	18.0	32.0	0.81
2	L	39.80	46.05	18.0	30.1	0.86
	T	38.50	46.38	17.5	30.0	0.83
	X	38.41	45.74	18.0	31.4	0.84
3	L	39.37	47.46	18.8	32.2	0.83
	T	42.35	48.76	19.0	32.6	0.87
	X	41.52	47.92	18.5	33.9	0.86

Table 2(b) Tensile properties of steel plates of different heats (quarter-width position)

Heat No.	Orientation	Yield strength, kg/mm^2	Tensile strength, kg/mm^2	Uniform elongation, %	Total elongation on 50 mm GL, %	YS/UTS
1	L	41.87	51.73	17.5	29.6	0.81
	T	44.77	52.13	16.0	26.7	0.86
	X	43.62	52.56	18.0	30.0	0.83
2	L	39.63	46.28	18.0	30.7	0.85
	T	38.34	46.62	17.5	30.2	0.82
	X	39.42	46.06	18.0	31.0	0.85
3	L	40.51	48.32	19.3	32.8	0.85
	T	40.34	46.33	18.6	32.2	0.87
	X	40.14	46.02	19.6	33.8	0.87

through the basic oxygen furnace continuous-casting route and subsequently hot rolled in a hot-strip mill. Heat 1 was argon purged, whereas heats 2 and 3 were treated with Ca-Mg powder for desulfurization as well as for sulfide shape control.

Tensile tests were carried out on flat specimens taken from the half- and quarter-width positions of each plate, and properties such as yield strength, tensile strength, uniform elongation, and total elongation were determined in the longitudinal (L), transverse (T), and 45° (X) orientations to the rolling direction. The tensile specimens were of 50 mm gage length (GL) and 12.5 mm width and were ground finished. Tensile testing was carried out on a 10 ton static universal testing machine model: INSTRON-1195 (Instron Limited, High Wycombe, Bucks, UK) at a crosshead speed of 5 mm/min. During testing, a 50 mm extensometer was used until fracture occurred. The tensile properties of the steel plates corresponding to the half- and quarter-width locations are compiled in Tables 2(a) and 2(b), respectively, for all three heats.

The CVN impact energy of plates from each steel heat was evaluated for half-size specimens (10 by 5 by 55 mm) at various test temperatures (ambient to –90 °C) in both the longitudinal and transverse directions. Tables 3(a) and 3(b) show the CVN impact properties of plates corresponding to the half- and quarter-width positions, respectively. Each data point, as reported in these tables, corresponded to the average of five best matching values obtained for that particular set.

The microstructures of the plate samples from all three heats were observed in the longitudinal through-thickness (LT) direction, and the average grain diameters were measured from the micrographs using the linear-intercept method. The ASTM grain sizes corresponding to these average grain diameters were determined from standard tables. For the metallographic study of nonmetallic inclusions, samples were also examined in the LT direction, corresponding to the half- and quarter-width locations of each plate. These samples were hardened by austenitizing at 900 °C for 30 min and oil quenched to prevent inclusion pullout during polishing. The hardened samples were polished to a scratch-free metallographic finish and examined in the optical microscope to observe nonmetallic inclusion distributions and characteristics.

The volume fractions of pearlite and nonmetallic inclusions were determined for all the plate steels by quantitative image analysis (QIA). Qualitative electron probe microanalysis (EPMA) was carried out to determine the chemistry of inclusion species present in each of the plate samples. In addition, the fracture surfaces of both tensile and impact-tested specimens were examined by scanning electron microscopy (SEM) to observe topographic features and associated fracture modes.

Table 3(a) Charpy V-notch impact properties of hot-rolled steel plates of different heats (half-width position)

Heat No.	Orientation	CVN impact energy, kg · m/cm², at different temperatures, °C								
		20	0	-15	-30	-45	-60	-75	-80	-90
1	L	12.57	12.37	11.97	11.43	10.94	10.51	10.05	9.50	6.95
	T	3.59	3.56	3.54	3.30	3.25	2.90	1.75	1.67	0.96
2	L	29.90	...	29.90	29.50	28.30	27.40	25.38	...	22.10
	T	21.85	...	21.75	20.66	19.10	17.34	13.52	...	11.05
3	L	29.42	...	28.63	28.36	26.76	25.19	24.96	...	12.53
	T	22.88	...	22.20	21.97	19.83	18.54	17.44	...	10.75

Table 3(b) Charpy V-notch impact properties of hot-rolled steel plates of different heats (quarter-width position)

Heat No.	Orientation	CVN impact energy, kg · m/cm², at different temperatures, °C								
		20	0	-15	-30	-45	-60	-75	-80	-90
1	L	12.33	12.10	11.90	11.74	11.15	10.71	10.30	9.97	7.39
	T	3.52	3.50	3.50	3.50	3.35	3.14	3.00	2.92	1.24
2	L	29.55	...	28.98	28.45	26.86	26.57	24.53	...	20.47
	T	21.52	...	20.90	20.34	18.25	16.62	12.63	...	10.18
3	L	28.56	...	28.26	26.52	25.17	22.91	20.31	...	11.01
	T	22.52	...	20.52	19.16	17.29	16.38	13.72	...	9.71

Table 4(a) Microstructural features of hot-rolled steel plates of different heats

Heat No.	Pearlite volume, %	Grain size	
		Average diameter, μm	ASTM No.
1	13.04	6.80	11-12
2	7.20	6.79	11-12
3	8.24	6.12	11-12

Table 4(b) Inclusion characteristics of hot-rolled steel plates of different heats

Heat No.	Inclusion volume fraction, %		Types of inclusions
	Half-width location	Quarter-width location	
1	0.26	0.30	Mostly MnS stringers. Al_2O_3 particles either isolated or in clusters. Isolated Al_2O_3 particles occasionally found enveloped by MnS
2	0.09	0.10	Very clean steel. Small oxysulfide inclusions of lenticular shape, with distinct oxide and sulfide phases
3	0.12	0.14	Clean steel with mostly globular oxysulfide inclusions

3. Results and Discussion

3.1 *Microstructure*

The nital-etched microstructures of as-rolled plate samples in the LT direction are shown for all the heats in Fig. 1. The microstructures are essentially ferritic, with minor amounts of pearlite. The microstructural features observed at the half- and quarter-width locations of each plate sample were found to be identical.

The volume fraction of pearlite determined by QIA methods was 13.04% for heat 1, which incidentally contains higher carbon (0.12 wt%) than heats 2 (0.08 wt%) and 3 (0.09 wt%). In addition, slightly pancake-shaped ferrite grains indicative of incomplete recrystallization in the through-thickness direction, parallel arrays of thin and elongated MnS stringers cutting across ferrite grains, and banding tendency of pearlite were observed (Fig. 1a) in this sample. In plate samples of heats 2 and 3, the volume fractions of pearlite determined by QIA methods were 7.20 and 8.24%, respectively, which is in agreement with their carbon contents. In plate samples of heat 2, ferrite and pearlite distribution (Fig. 1b) was random and the grains comparatively equiaxed. The microstructure of heat 3 plate samples (Fig. 1c), despite also displaying equiaxed ferrite as in heat 2, exhibited comparatively greater banding tendency than that observed in heat 1 plate samples. Banding is known to be caused primarily by the interdendritic segregation of manganese during solidification. The manifestations of pearlite banding in plate samples of heats 1 and 3 can thus be attributed to their comparatively high manganese contents (0.96 and 1.25 wt%, respectively). The relatively more pronounced evidence of pearlite banding in heat 3 as compared to heat 1 thus can presumably be attributed to its higher manganese content (1.25 wt%). Interestingly, the plate sample of heat 2 with the lowest manganese content (0.51%) showed no evidence of banding.

The average grain diameters determined by the linear-intercept method as well as the corresponding ASTM grain size numbers (Table 4a) were found to be similar (ASTM no. 11 to 12) in plate samples of all three heats.

3.2 *Inclusion Characteristics*

The typical inclusion fields observed in plate samples of all three heats are shown in Fig. 2. In plate samples of heat 1, the

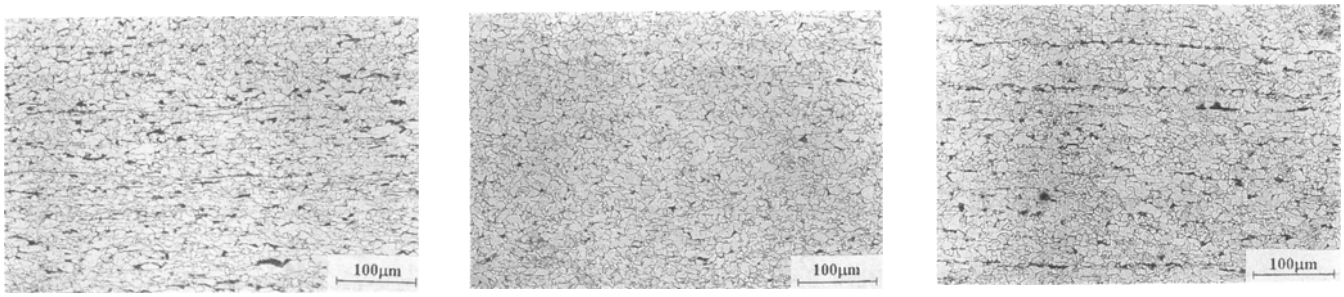

Fig. 1 Optical micrographs showing ferrite and pearlite distributions in different steel plates. (a) Heat 1. (b) Heat 2. (c) Heat 3

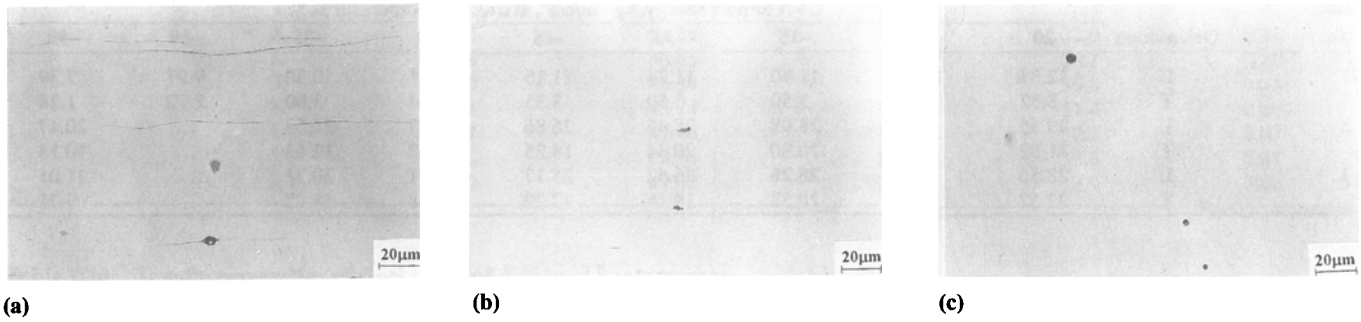

Fig. 2 Optical micrographs of typical inclusions in different steel plates. (a) Heat 1. (b) Heat 2. (c) Heat 3

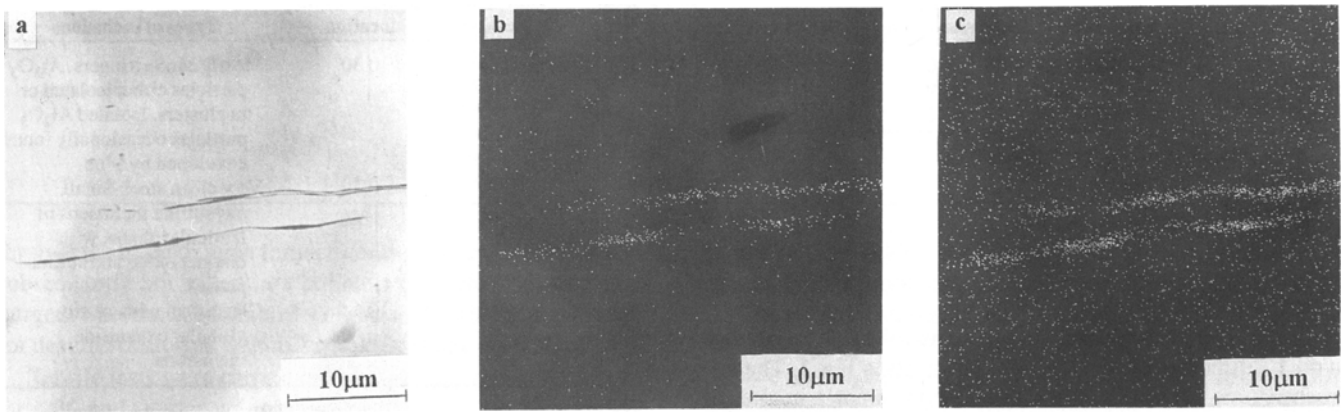

Fig. 3 Qualitative microprobe analysis of typical sulfide stringers in plates of heat 1. (a) Backscattered electron image. (b) Sulfur x-ray map. (c) Manganese x-ray map

inclusions were predominantly MnS stringers. Aluminum oxide inclusions, either isolated or in clusters, were also observed in some regions. In some cases, the Al_2O_3 particles were enveloped by MnS. Electron probe microanalysis scans of a typical MnS stringer showing backscattered electron and x-ray mapping images of sulfur and manganese are presented in Fig. 3.

Heats 2 and 3, which were treated with Ca-Mg powder for desulfurization as well as for sulfide shape control, were found to be cleaner than heat 1 (Table 4b) from the standpoint of inclusion volume fraction. An optical micrograph of typical inclusions observed in heat 2 is shown in Fig. 2(b). These small lenticular inclusions, when observed at higher magnifications in the EPMA, were found to be essentially oxysulfides with distinct oxide and sulfide phases. Figure 4 shows qualitative EPMA of such an inclusion, as depicted by backscattered electron and x-ray mapping images. The dark oxide phase (Fig. 4a) was found to be mainly Al_2O_3 with small amounts of calcium and magnesium, whereas the light gray sulfide phase (Fig. 4a) was essentially MnS with small amounts of calcium and magnesium. The backscattered electron image confirms that the sulfide inclusions in heat 2 are lenticular in shape and often precipitated along with oxides.

The optical micrograph of a typical field showing small globular inclusions in the plate sample of heat 3 (Fig. 2c) is indicative of complete sulfide shape control. Electron probe microanalysis scans (Fig. 5) showed that these globular inclusions were oxysulfides containing aluminum, calcium, magnesium, oxide, sulfur, and manganese. Distinct phase delineation (ox-

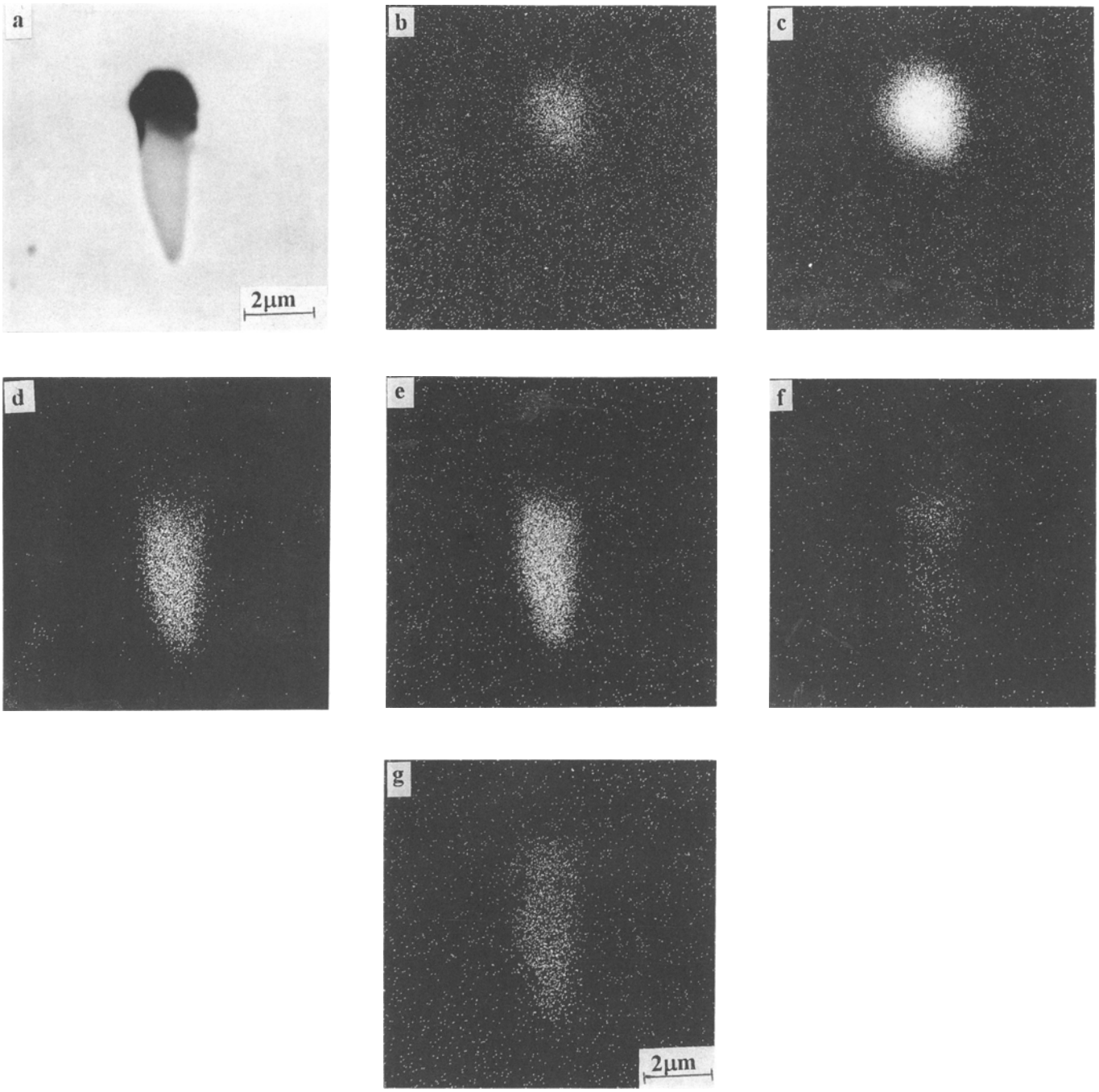

Fig. 4 Qualitative microprobe analysis of lenticular oxysulfide inclusions in plates of heat 2. (a) Backscattered electron image. (b) Oxide x-ray map. (c) Aluminum x-ray map. (d) Sulfur x-ray map. (e) Manganese x-ray map. (f) Magnesium x-ray map. (g) Calcium x-ray map

ide, black, sulfide, gray) was observed within these globular inclusions as manifested in the backscattered electron image (Fig. 5a).

Quantitative image analysis data of inclusion volume fraction determined for the half- and quarter-width plate locations of each heat are shown in Table 4(b). The inclusion volume fractions were found to be similar for both locations in each plate sample. From the standpoint of cleanliness, however, plate samples of heats 2 and 3 exhibited much lower inclusion volume fractions (0.09 and 0.12%, respectively) than did heat 1 (0.26%).

3.3 *Tensile Properties*

The room-temperature tensile properties in the L, T, and X directions of the three plate steels, corresponding to half- and quarter-width positions, are shown in Tables 2(a) and 2(b), respectively. For any particular heat, no significant variation in tensile properties was observed between samples of half- and quarter-width locations. Besides, the yield and tensile strength values specific to any heat were found to be unaffected by specimen orientation. The heat-to-heat variations in strengths

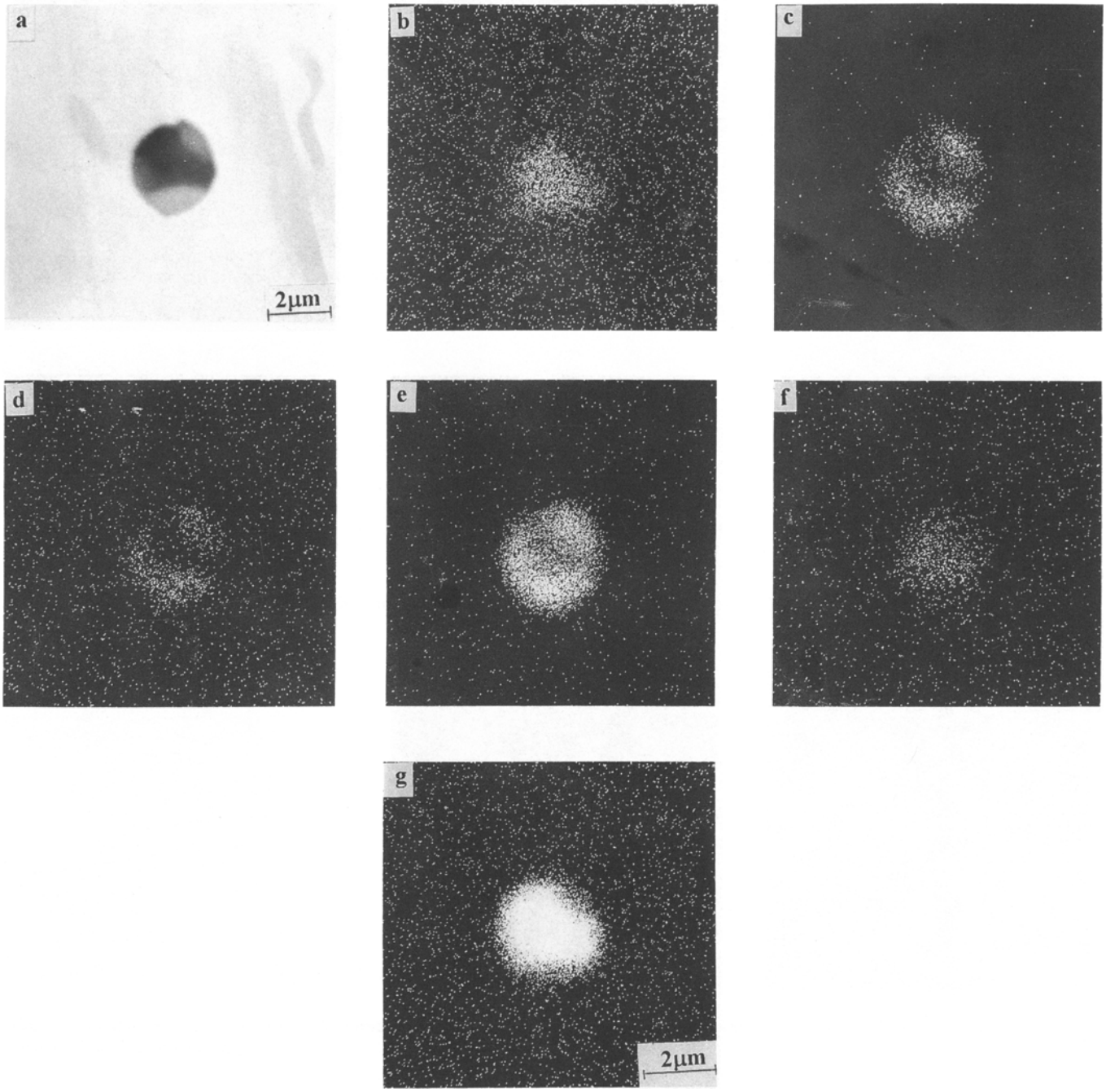

Fig. 5 Qualitative microprobe analysis of globular oxysulfide inclusions in plates of heat 3. (a) Backscattered electron image. (b) Oxide x-ray map. (c) Sulfur x-ray map. (d) Manganese x-ray map. (e) Calcium x-ray map. (f) Magnesium x-ray map. (g) Aluminum x-ray map

could, however, be attributed to differences in chemistry rather than to inclusion characteristics. The effect of unfavorable inclusion morphology in reducing transverse tensile ductility, as indicated by total elongation values, was evident in heat 1, which exhibited a preponderance of MnS stringers. The total elongation values listed in Tables 2(a) and 2(b) for heat 1 plates were 3 to 5% lower for transverse-orientation specimens than for longitudinal specimens. The anisotropy in transverse ductility has been shown to be minimal after sulfide shape control (Ref 7, 8). With sulfide shape control, tensile specimens of plates from heats 2 and 3 exhibited virtually identical longitudinal and transverse ductility as measured by total percentage elongation. The present study therefore corroborates the beneficial effect of sulfide shape control in minimizing tensile anisotropy.

Figure 6 presents SEM images showing the fracture topography of transverse-orientation tensile-tested specimens of all three heats. The fracture surfaces of all the samples consist of larger dimples separated by regions of fine dimple arrays. This topography is characteristic of ductile fracture where non-

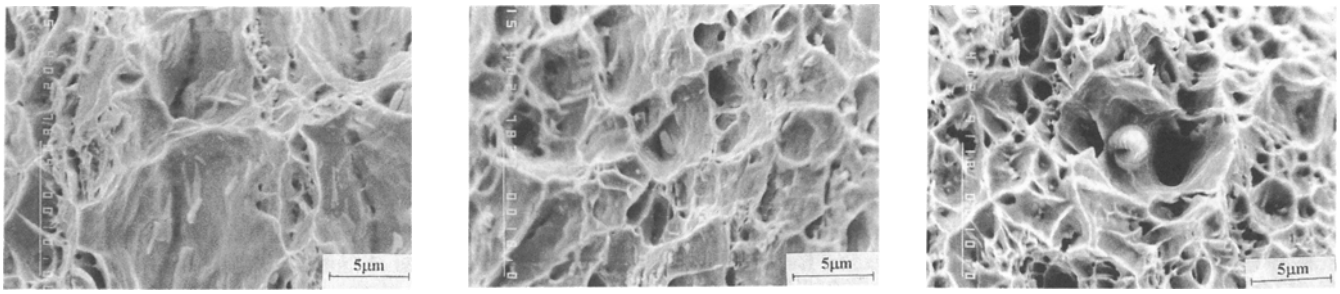

(a) (b) (c)

Fig. 6 Scanning electron fractographs of transverse tensile samples. (a) Heat 1 with shattered MnS stringers inside large voids. (b) Heat 2 with tiny lenticular sulfides inside smaller voids. (c) Heat 3 with globular oxysulfide inclusions inside large voids

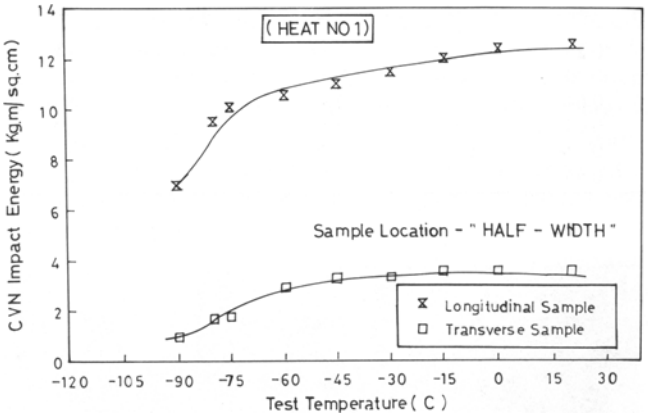

Fig. 7 Variation of CVN impact energy with temperature for plate samples of heat 1 taken from the half-width position

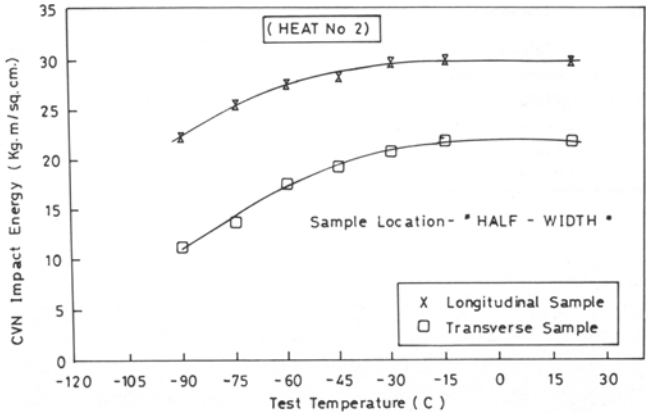

Fig. 8 Variation of CVN impact energy with temperature for plate samples of heat 2 taken from the half-width position

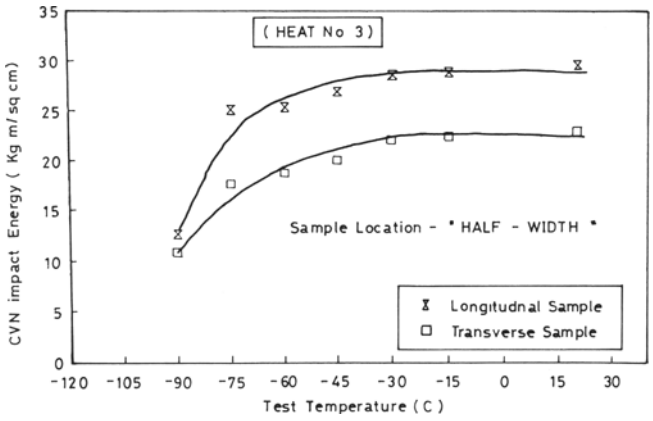

Fig. 9 Variation of CVN impact energy with temperature for plate samples of heat 3 taken from the half-width position

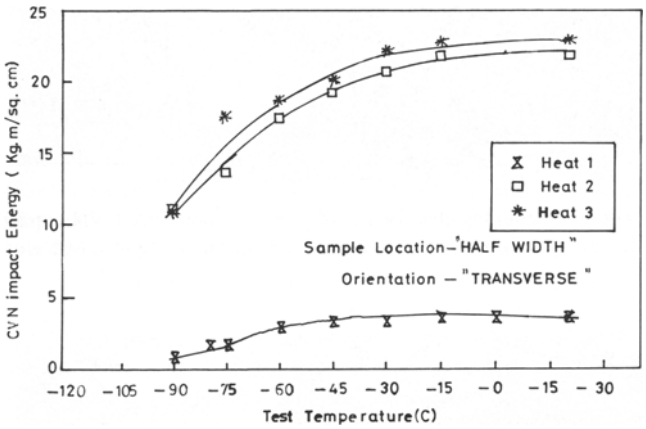

Fig. 10 Composite plot showing variation of CVN impact energy with temperature for transverse specimens of heats 1 to 3 taken from the half-width position

metallic inclusions are responsible for nucleating voids. The fractograph of a transverse-orientation tensile-tested specimen of heat 1 (Fig. 6a) reveals very large voids with shattered MnS inclusions inside them. In the case of heat 2, the tensile fracture surface exhibits smaller voids with tiny lenticular sulfides at the bottom (Fig. 6b). The tensile fracture surface of a sample from heat 3 reveals globular oxysulfides inside the voids (Fig. 6c). All the fractographs illustrate the dominant morphologies of inclusions unique to each steel heat.

3.4 *Impact Properties*

The CVN impact properties of longitudinal and transverse specimens, corresponding to half- and quarter-width positions of the plates from each heat, were determined at various test temperatures and are listed in Tables 3(a) and 3(b), respectively. For any particular heat and test temperature, no significant difference in impact energy values was observed for samples from both locations.

The CVN impact curves for longitudinal and transverse specimens corresponding to the half-width locations of plates are shown in Fig. 7 to 9 for heats 1 to 3, respectively. It is clearly evident that the shelf-energy values in the longitudinal direction are greater than those in the transverse direction for any specific heat and test temperature. The difference between the longitudinal and transverse shelf-energy values, however, is more pronounced for heat 1 than for heats 2 and 3. The variation of CVN impact energy with test temperature for transverse-orientation specimens of all three heats is shown as a composite plot in Fig. 10. It can be seen that, regardless of specimen orientation or test temperature, the shelf energies of impact specimens of heats 2 and 3 are considerably higher than those of heat 1. The plots (Fig. 7 to 10) also show that ITT was attained (–80 °C) only for the transverse specimens of heat 1; those of heats 2 and 3 exhibited no ITT up to –90 °C. The macroscopic appearance of broken impact specimens indicated that 50% brittle fracture was obtained for transverse specimens of

Table 5 CVN impact energy ratios in hot-rolled steel plates of different heats at various temperatures

Heat		Impact energy ratio (t/L) at different temperatures, °C								
No.	Location	20	0	–15	–30	–45	–60	–75	–80	–90
1	Half-width	0.29	0.29	0.29	0.29	0.29	0.25	0.17	0.17	0.14
	Quarter-width	0.29	0.29	0.29	0.30	0.30	0.29	0.29	0.29	0.17
2	Half-width	0.73	...	0.72	0.70	0.67	0.63	0.53	...	0.50
	Quarter-width	0.73	...	0.72	0.71	0.68	0.62	0.51	...	0.50
3	Half-width	0.78	...	0.77	0.77	0.74	0.74	0.70	...	0.55
	Quarter-width	0.79	...	0.73	0.72	0.69	0.71	0.67	...	0.88

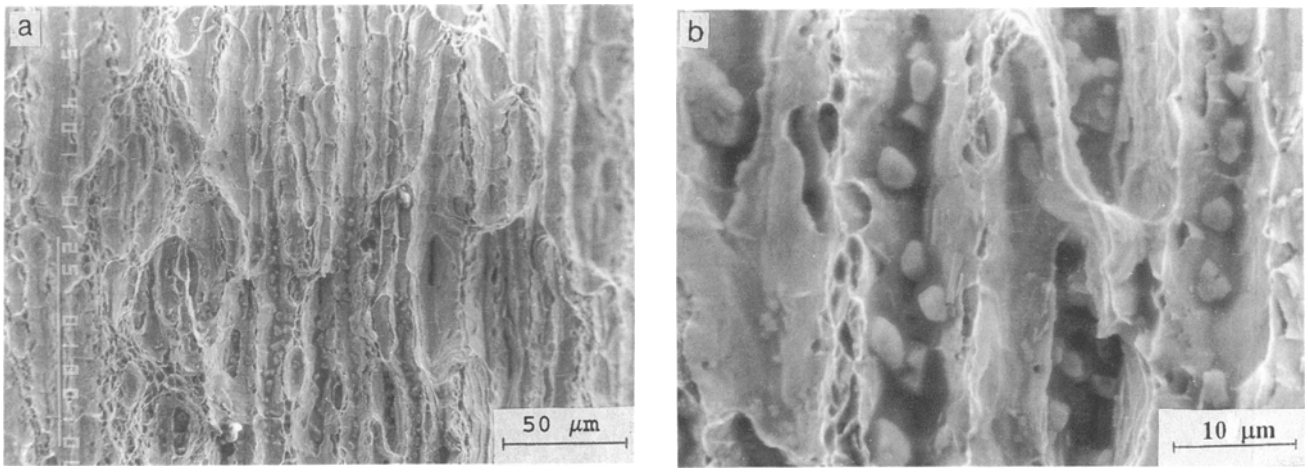

Fig. 11 Scanning electron fractographs of transverse CVN impact specimen from heat 1 showing splitting. (a) Fracture surface with parallel arrays of splits. (b) Localized inclusion clustering in split furrows

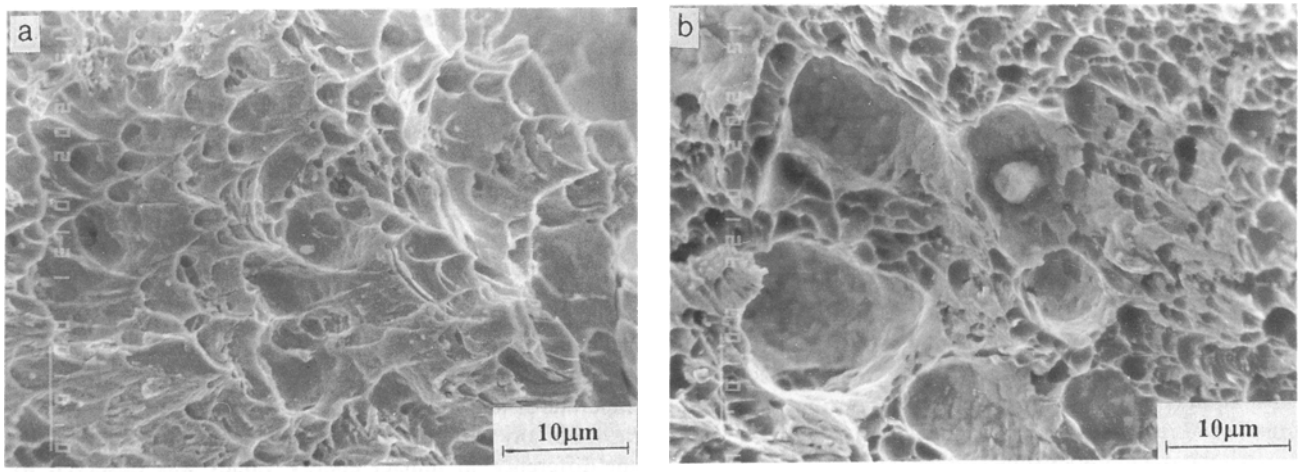

Fig. 12 Scanning electron fractographs of transverse CVN impact specimens showing dimple ductile fracture. (a) Heat 2. (b) Heat 3

heat 1. On the contrary, transverse specimens of heats 2 and 3 showed complete ductility even at –90 °C. This also confirms the earlier findings that ITT in the transverse direction is greater than in the longitudinal direction.

The effect of inclusion cleanliness n Charpy shelf energy is clearly evident in Fig. 7 to 9. Heats 2 and 3, being cleaner than heat (Table 4b), exhibited substantially greater impact values (more than twice in the longitudinal and five times in the transverse direction). As a matter of fact, transverse specimens of heats 2 and 3 exhibited ten times greater impact energy values than did heat 1 samples at test temperatures below –60 °C. However, such differences in impact values may also be attributable to factors other than cleanliness level. It has been reported that increased pearlite content reduces shelf energy (Ref 1). The microstructural features (Table 4a) of the steel investigated show that the pearlite volume fraction in heat 1 (13.04%) was about 1.8 and 1.6 times greater than the pearlite contents of heats 2 and 3, respectively. Thus, the low CVN shelf energy in heat 1 can be attributed to the combined effect of increased pearlite and inclusion contents. In addition, manifestations of pearlite banding in heat 1 may have also contributed to lowering the shelf energy.

The anisotropy in the CVN impact energy (transverse-to-longitudinal energy ratio) for all three heats is shown in Table 5. The shelf energy in the transverse direction (Fig. 10) was lowest for heat 1. The preponderance of elongated MnS inclusions in this heat resulted in maximum anisotropy (0.29 at ambient temperature). With sulfide shape control, as in heats 2 and 3, the transverse impact energies improved significantly with respect to the longitudinal direction, and anisotropy was minimized. Heat 3, despite pearlite banding and a greater inclusion volume fraction, exhibited less anisotropy (0.79 at 20 °C) than heat 2 (0.73 at 20 °C) (which, incidentally, was devoid of banding and contained a lower inclusion content). The low anisotropy of heat 3 can therefore be attributed to the complete globurization of sulfide (Fig. 5a), in contrast to the partial sulfide shape control and the lenticular sulfide morphology (Fig. 4a) obtained in heat 2. These findings indicate that anisotropy of impact properties is more sensitive to inclusion morphology than to pearlite banding.

The fracture topography of transverse CVN impact specimens of heat 1 tested at room temperature showed parallel arrays of splits (Fig. 11), whereas ductile dimples (Fig. 12) were observed in specimens of heats 2 and 3. The split-type fracture surface of an impact-tested specimen of heat 1 (Fig. 11b) clearly revealed ridges and valleys. The ridges were seen to be associated with ductile dimples, whereas the valleys or furrows exhibited a relatively smooth surface, indicative of failure by a low-energy mode. The presence of oxide stringers and sulfide inclusions inside these furrows lends credence to their role in splitting as well as in the nucleation of microvoids, resulting in very low impact energy values.

Bramfitt and Marder (Ref 11) have also observed such splitting phenomena in Charpy-tested low-carbon steel specimens containing pancake-shaped ferrite grains parallel to the rolling plane. Incidentally, the microstructure of heat 1 plate samples (Fig. 1) revealed that the grains had a tendency to take on a pancake shape in the through-thickness rolling direction, as opposed to heats 2 and 3 where the ferrite grains were comparatively equiaxed. The role of elongated MnS inclusions in inhibiting ferrite grain growth in the through-thickness direction and thereby resulting in the formation of pancake-shaped ferrite grains has been reported (Ref 12). Moreover, elongated sulfides also allow easier matrix-inclusion decohesion because of their larger area of contact with the matrix. Thus, the low impact energy of heat 1 plates, which could not be earlier explained merely by the volume fraction of nonmetallic inclusions, has presumably also been influenced by the pancake-shaped ferrite grains, which have resulted in the splitting phenomenon.

4. Conclusions

Although the 7 mm thick hot-rolled plates of all three heats exhibited similar grain sizes, pancaked-shaped ferrite grains indicative of incomplete recrystallization in the through-thickness direction were observed only in plates containing stringer sulfides.

The absence of such a feature in sulfide shape-controlled heats confirms the role of elongated MnS inclusions in inhibiting equiaxed grain formation.

Pearlite banding was observed in plates of heats 1 and 3, and its relative severity was in direct agreement with their high manganese contents. The absence of such banding in heat 2, which had a lower manganese but a similar carbon content as heat 3, corroborates the role of manganese in enhancing banding propensity.

Although yield and tensile strengths specific to any heat were unaffected by specimen orientation, anisotropy in tensile ductility, as measured by total elongation, was exhibited only by plates containing MnS stringers. Elongated MnS stringers have been found to reduce total elongation of transverse specimens by 3 to 5%, whereas such anisotropy is absent in sulfide shape-controlled heats.

Charpy V-notch impact energies, regardless of specimen orientation and test temperatures, were significantly greater in cleaner steels. The lowest impact energy, obtained in heat 1 plate samples, was influenced by a higher pearlite volume fraction (as well as by inclusion content and morphology).

Pancake-shaped ferrite grains, typical of heat 1 specimens containing MnS stringers, drastically reduced transverse impact energy because of their tendency to promote splitting. The absence of such splitting in sulfide shape-controlled heats with equiaxed ferrite confirmed this phenomenon.

Impact transition temperature was obtained only for transverse specimens of heat 1 containing MnS stringers, while cleaner and shape-controlled heats with lower pearlite volume fractions did not exhibit ITT up to –90 °C. The preponderance of MnS stringers in heat 1 was therefore presumably responsible for the ITT being greater in the transverse direction than in the longitudinal direction.

Anisotropy of impact energy was found to be more sensitive to inclusion morphology than to pearlite banding. The anisotropy decreased in the following order: heats 1, 2, and 3. The highest anisotropy, exhibited by heat 1, was attributed to the high incidence of MnS stringers; the lowest, in heat 3, to complete globurization of MnS. The relatively insignificant influence of pearlite banding on anisotropy is testified to by heat 3,

which despite containing banded pearlite, exhibited lower anisotropy than band-free heat 2, which contained lenticular sulfides.

Acknowledgments

The authors are grateful to Dr. S. Banerjee, Director, Research and Development Centre for Iron and Steel, Steel Authority of India Limited, for his encouragement and support. Thanks are specially due to Mr. B.B. Patra and Mr. John Guria for their help in the investigation.

References

1. W.A. Spitzig and R.J. Sober, Influence of Sulfide Inclusions and Pearlite Content on the Mechanical Properties of Hot-Rolled Carbon Steels, *Metall. Trans. A*, Vol 12A (No. 2), 1981, p 281-291
2. I. Kozasu, T. Shimizu, and H. Kubota, The Effect of Nonmetallic Inclusions on the Ductility and Toughness of Structural Steels, *Trans. Iron Steel Inst. Jpn.*, Vol 13 (No. 1), 1973, p 20-28
3. T. Gladman, B. Holmes, and I.D. McIvor, Effects of Second Phase Particles on Strength, Toughness and Ductility, *Effect of Second Phase Particles on the Mechanical Properties of Steel*, Iron and Steel Institute, London, 1971, p 68-78
4. T.J. Baker, K.B. Gove, and J.A. Charles, Inclusion Deformation and Toughness Anisotropy in Hot-Rolled Steels, *Met. Technol.*, April 1976, p 183-193
5. W. Dahl, H. Hengstenberg, and C. Duren, Behavior of Different Types of Sulphides during Shaping and Their Effect on the Mechanical Properties, *Stahl Eisen*, Vol 86 (No. 13), 1966, p 796-817
6. I. Kozasu and H. Kubota, The Effect of Elongated Sulphide Inclusions on Ductility and Ductile Fracture of a Structural Steel, *Trans. Iron Steel Inst. Jpn.*, Vol 11 (No. 5), 1971, p 321-330
7. L. Luyckx, J.R. Bell, A. McLean, and M. Korchynsky, Sulphide Shape Control in High Strength Low Alloy Steels, *Metall. Trans.*, Vol 1, 1970, p 3341-3350
8. S.K. Pal and S. Mishra, Effect of Sulphide Shape Control on the Formability and Fracture Behavior of a High-Strength Low-Alloy Steel, *Met. Mater. Process.*, Vol 4 (No. 3), 1992, p 189-202
9. G.R. Speich and W.A. Spitzig, Effect of Volume Fraction and Shape of Sulfide Inclusions on Through-Thickness Ductility and Impact Energy of High-Strength 4340 Plate Steels, *Metall Trans. A*, Vol 13A (No. 12), 1982, p 2239-2258
10. F.B. Pickering, in *Proc. Symp. Toward Improved Ductility and Toughness* (Kyoto), Climax Molybdenum Development Company, 1971, p 9
11. B.L. Bramfitt and A.R. Marder, *Metall. Trans. A*, Vol 8A, 1977, p 1263-1273
12. R.D. Knutsen and R. Hutchings, Occurrence of Non-Metallic Inclusions in 3 CR 12 Steel and Their Effect on Impact Toughness, *Mater. Sci. Technol*, Vol 4 (No. 2), 1988, p 127-135